AD-A031 204 NAVAL RESEARCH LAB WASHINGTON D C F/G 20/9
THERMAL FORCE CONTRIBUTIONS TO SELF-GENERATED MAGNETIC FIELDS I--ETC(U)
SEP 76 D G COLOMBANT, N K WINSOR
UNCLASSIFIED NRL-MR-3362 NL

1 OF 1
AD A031204

END
DATE FILMED
11-76

NRL Memorandum Report 3362

Thermal Force Contributions to Self-Generated Magnetic Fields in Laser-Produced Plasmas

D. G. COLOMBANT

Science Applications, Inc.
McLean, Virginia 22101

and

N. K. WINSOR

Plasma Dynamics Branch
Plasma Physics Division

September 1976

NAVAL RESEARCH LABORATORY
Washington, D.C.

SECURITY CLASSIFICATION OF THIS PAGE (When Data Entered)

REPORT DOCUMENTATION PAGE

READ INSTRUCTIONS BEFORE COMPLETING FORM

1. REPORT NUMBER: NRL ~~Memorandum Report~~ 3362	2. GOVT ACCESSION NO.
3. RECIPIENT'S CATALOG NUMBER	
4. TITLE (and Subtitle): THERMAL FORCE CONTRIBUTIONS TO SELF-GENERATED MAGNETIC FIELDS IN LASER-PRODUCED PLASMAS	5. TYPE OF REPORT & PERIOD COVERED: Interim report on a continuing ~~NRL problem~~.
	6. PERFORMING ORG. REPORT NUMBER
7. AUTHOR(s): D.G. Colombant ~~and~~ N.K. Winsor	8. CONTRACT OR GRANT NUMBER(s): —
9. PERFORMING ORGANIZATION NAME AND ADDRESS: Naval Research Laboratory, Washington, D.C. 20375	10. PROGRAM ELEMENT, PROJECT, TASK AREA & WORK UNIT NUMBERS: NRL ~~Problem~~ H02-29B
11. CONTROLLING OFFICE NAME AND ADDRESS: University of Rochester, Rochester, New York and Office of Naval Research, Arlington, Virginia 22217	12. REPORT DATE: Sept~~ember~~ 1976
	13. NUMBER OF PAGES: 21
14. MONITORING AGENCY NAME & ADDRESS(if different from Controlling Office)	15. SECURITY CLASS. (of this report): UNCLASSIFIED
	15a. DECLASSIFICATION/DOWNGRADING SCHEDULE

16. DISTRIBUTION STATEMENT (of this Report)

Approved for public release; distribution unlimited.

17. DISTRIBUTION STATEMENT (of the abstract entered in Block 20, if different from Report)

18. SUPPLEMENTARY NOTES

19. KEY WORDS (Continue on reverse side if necessary and identify by block number)

Laser
Plasma
Magnetic field
Theory

20. ABSTRACT (Continue on reverse side if necessary and identify by block number)

The several magnetic source terms affecting laser-produced plasmas are presented and their importance discussed. The thermal force is shown to greatly modify the magnetic field distribution. The hard X-ray spectrum is quantitatively compared with the experiment.

DD FORM 1 JAN 73 1473 EDITION OF 1 NOV 65 IS OBSOLETE
S/N 0102-014-6601

SECURITY CLASSIFICATION OF THIS PAGE (When Data Entered)

251950

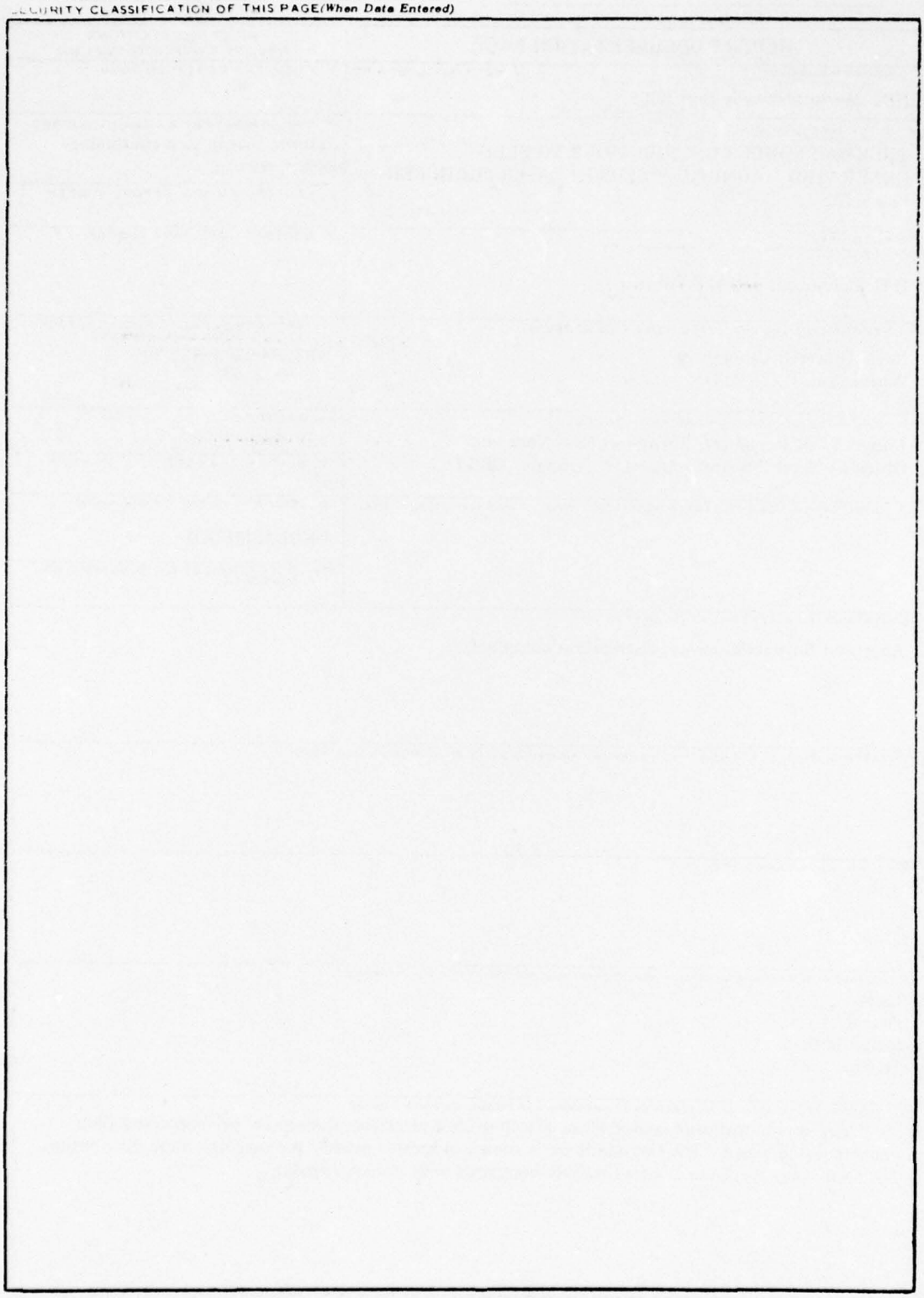

CONTENTS

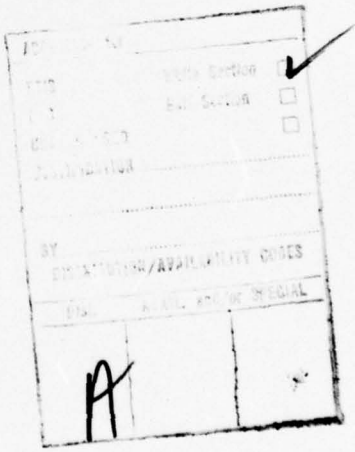

THERMAL FORCE CONTRIBUTIONS TO SELF-GENERATED MAGNETIC FIELDS IN LASER-PRODUCED PLASMAS

Section 1

1.0 INTRODUCTION

In a previous publication[1], we have shown the crucial importance of magnetic fields in the interpretation of continuum x-ray spectra obtained when high Nd laser intensities ($10^{16} W/cm^2$) interact with plane solid targets. In this paper, we present more detailed numerical results from a more complete model. We analyze the contributions of the various thermal magnetic field source terms; we find that although the magnetic field represents only a very small fraction of the deposited laser energy, the influence of the B field can be drastic on the transport coefficients and can in turn affect the overall redistribution of energy in the plasma produced right in front of the target. Section II describes the complete B-field equation used in the two-dimensional numerical model, Section III recalls the main features of the model and the initial conditions; Section IV consists of the results to the B-field equation and finally Section V summarizes the central features of the solution and shows its influence on the continuum x-ray spectrum.

Note: Manuscript submitted August 26, 1976.

Section 2

2.0 MAGNETIC FIELD EQUATION

The B-field is derived from the electric field which is itself derived from the generalized Ohm's law. All terms except $\partial j/\partial t$ are left in Ohm's law so that the full B-equation reads:

$$\frac{\partial B}{\partial t} = \nabla x \left[VxB - \frac{c^2}{4\pi} \underset{\sim}{\eta} \cdot (\nabla xB) \right] - \frac{ck}{eN_e} \nabla N_e x \nabla T_e$$

$$- \frac{c}{4\pi e} \nabla x \frac{1}{N_e} (\nabla xB) \, xB - \frac{c}{e} \nabla x \frac{(\beta_\perp \nabla T_e - \beta_\wedge \hat{b} x \nabla T_e)}{N_e} \qquad (1)$$

where V is the fluid velocity, $\underset{\sim}{\eta}$ the resistivity tensor, N_e the electron density, T_e the electron temperature and the β's are coefficients depending on $\omega_{ce}\,\tau_{ei}$ and defined in Braginski[2]. The only assumptions made in deriving Eq. (1) are that the electron pressure is isotropic and that the ponderomotive force effects have not been included in the electric field.

The last term on the right-hand side of Eq.(1) corresponds to the thermal force which arises due to the unbalance of the friction force on electrons in presence of a thermal gradient. This term enters the expression for the electric field as $- \frac{\underset{\sim}{R_T}}{eNe}$ and also the energy equation as $- \frac{\underset{\sim}{R_T}}{eNe} \cdot j$ where $R_T = \beta_\perp \nabla Te - \beta_\wedge \hat{b} x \nabla Te$.

A short analysis of the terms in Eq.(1) will help with the interpretation of the results which are presented further down. The third term on the right hand side for example is very similar in nature to the second one if we neglect the term due to curvature of the B-field. It can then be written as

$$- \frac{c}{4\pi e} \nabla N_e^{-1} x \nabla \left(\frac{B^2}{8\pi} \right)$$

So, only when $B^2/8\pi$ becomes large compared to P_e, this term becomes important.

As for the thermal force term, because the β's are proportional to the B field, it can be seen readily that the spontaneous magnetic field will grow first due to the $\nabla N_e \times \nabla T_e$ term. Only when $(\omega_{ce}\tau_{ei})$ becomes of order one, the thermal force terms become important and in fact compete with the electron pressure source term. It is expected then that the thermal force term alters the magnetic field significantly once the B field has reached a magnitude so that the electron gyrofrequency is comparable to the electron-ion collision frequency. This thermal force term being a collisional term, the condition for its use will be that the electron-ion collision mean free path must be smaller than the mesh size. If we take for

$$\lambda_{m.f.p} = 1.44\ 10^{12}\ \frac{T_e^2}{z^4 n}$$

where T_e is in eV, it can be seen that λ will be less than 12μ - the grid size used in the calculation - for $T_e \leq 36$ keV at the critical density for Z=6. We shall see that this condition is satisfied there but the thermal force term must be turned off in the underdense region.

Section 3

3.0 MODEL

Besides the magnetic field equation, the model consists of equations for the conservation of mass, momentum and energy in cylindrical coordinates as described in Reference 3. The target is perpendicular to the laser axis which is also the z axis. Absorption of laser light occurs via inverse bremsstrahlung for electron densities below critical and at the critical density for the remainder of the laser energy. One difference with Reference 3 is that the present model contains a radiation pressure term so that $\nabla \cdot P_r = \hat{e}_z P_\ell / c$ where P_ℓ is the absorbed laser power. There are no adjustable parameters in the code.

The only input quantities for the code are the laser pulse and the target material and initial configuration at t=0.

The laser pulse is Gaussian both in space and time with a FWHM of 21 psec, an energy of 1J and a focal spot radius of 12μ. The target material is carbon although runs with polyethylene were made which did not change the results appreciably. One of the restrictions brought by the use of an eulerian code such as the one used here is that the calculations cannot start with an infinitely steep gradient. So an initial density gradient with an e-folding length of 27μ was set up initially. This length was varied from 20μ to 41μ without bringing any significant changes in the solution.

Section 4

4.0 RESULTS

Profiles for the magnetic field at t=18, 36 and 88.5 psec are shown in Figures 1 to 3. The thermal force is not included in these calculations and the first figure corresponds to the plasma variables profiles shown in Figure 3 of Reference 1. The B field reaches its maximum value near the peak of the pulse - which takes place at t=17 psec - and keeps a value close to its maximum until after the end of the laser pulse. Changes in field polarization occur during that period of time as can be seen from the figures and are due to intricate structures of the temperature and density profiles in two-dimensions. It is also seen from Figure 3 especially that the field follows the fluid motion which is shown typically in Figure 4 and 5. From these last two figures, it is seen that the plasma expansion occurs at first towards the laser - which is located at the bottom of all figures - and spreads laterally only gradually whereas the maximum velocity of the plasma front increases to speeds of 10^8cm/sec (corresponding to energies of 62 keV for carbon ions).

In Figures 6, 7, and 8 the magnetic field contours corresponding to the same case are shown when the thermal force is retained in Eq. (1). From the comparison between this series of figures and the previous ones, we see that

a) the magnitude of the maximum field is reduced from 2.5 MG to about 1.3 MG.

b) the maximum B field occurs later in time when the thermal force is included and at a much larger radius (100μ vs. 12μ)

c) the change in polarity occurs much less and much later for the thermal force case.

Results a) and c) are expected from our analysis of the effects of the thermal force terms, namely their competition with the electron pressure source terms and their collisional nature leading to a more coherent picture overall.

The different components of the magnetic field source terms can be written:

$$\frac{\partial B}{\delta t} = \cdots \frac{c}{en} \frac{\partial n}{\partial r} \frac{\partial T}{\partial z} - \frac{\partial n}{\partial z} \frac{\partial T}{\partial r} + \frac{c}{e} \frac{\partial T}{\partial r} \frac{\partial \beta_\perp}{\partial z} + \frac{\partial \beta_\wedge}{\partial z} \frac{\partial T}{\partial z}$$

$$- \frac{\partial T}{\partial z} \frac{\partial \beta_\perp}{\partial r} + \frac{\partial}{\partial r} \beta_\wedge \frac{\partial T}{\partial r}$$

and are shown in Figure 9. They correspond to the case of Figure 6 and their variations are shown 12μ off axis, only between z=190 and z=320μ. Although the competition between them is strong, $\frac{\partial n}{\partial z} \frac{\partial T}{\partial r}$ is the dominant term followed by $\frac{\partial \beta_\perp}{\partial r} \frac{\partial T}{\partial z}$.

Let us note that the $\frac{\partial n}{\partial r} \frac{\partial T}{\partial z}$ term which comes directly from the setting of the artificial density gradient in front of the target- since the laser steepens the density profile and thus produces a positive $\frac{\partial n}{\partial r}$ - is always down by 1 order of magnitude from the dominant terms and in that respect, the initial density gradient set-up does not invalidate the calculations. Corresponding to these different various cases, no strong maximum temperature off-axis was observed as has been reported elsewhere [4,5]. One reason for this result is that in our own previous calculation where we found a maximum off-axis[5], the radial grid size was less than the focal spot radius; another reason is that when the thermal force is included, the maximum B-field is pushed radially outwards and heat can diffuse more easily out of the focal region.

Section 5

5.0 CONCLUSION

In both cases, with or without thermal force, the total magnetic field energy is several orders of magnitude (typically six) below the absorbed energy and it is interesting to note that although very little energy is converted into magnetic, this form of energy through the transport coefficients, control the repartition of absorbed energy (thermal, radiated and even kinetic as was seen in Figures 4 and 5).

The overall effects of the thermal force on a macroscopically measurable quantity like the continuum x-ray spectrum is shown in Figure 10 - along with the corresponding experimental spectrum[1]. The x-ray spectrum obtained when the thermal force is included is below that one obtained without the thermal force and then agrees better with the experiment. This improvement can be explained since the reduction in heat flow is less when the thermal force is included and then the maximum temperature reached in this run was 19 keV instead of 61 keV for the corresponding case without thermal force. The disagreement above 100 keV photon energy results from the fact that the electron should be treated as relativistic when it reaches that energy level. At lower photon energy, the coarse resolution used in the calculations did not bring out all the details of the maximum emission region located behind the critical density where both the density and temperature gradients are very steep and occur over one cell in our calculations.

ACKNOWLEDGEMENT

We would like to thank Dave Bailey of Lawrence Livermore Laboratory and Jess Christiansen of Culham Laboratory who suggested including the effects of the thermal force in laser-target calculations.

This work was supported in part by the Laboratory for Laser Energetics at the University of Rochester, and by the Office of Naval Research.

REFERENCES

1. B.H. Ripin, et al, Phys. Rev.Lett. p.34, 1313 (1975).
2. S.I. Braginski, in Reviews of Plasma Physics, edited by M.A. Leontovich (Consultants Bureau, New York, 1965), Vol. 1, p.205.
3. N.K. Winsor and D.A. Tidman, Phys. Rev. Lett. p.31, 1044 (1973).
4. R.S. Craxton and M.G. Haines, Phys. Rev. Lett. p.35, 1336 (1975).
5. D.G. Colombant, et al, Phys. Fluids 18, 1687 (1975).

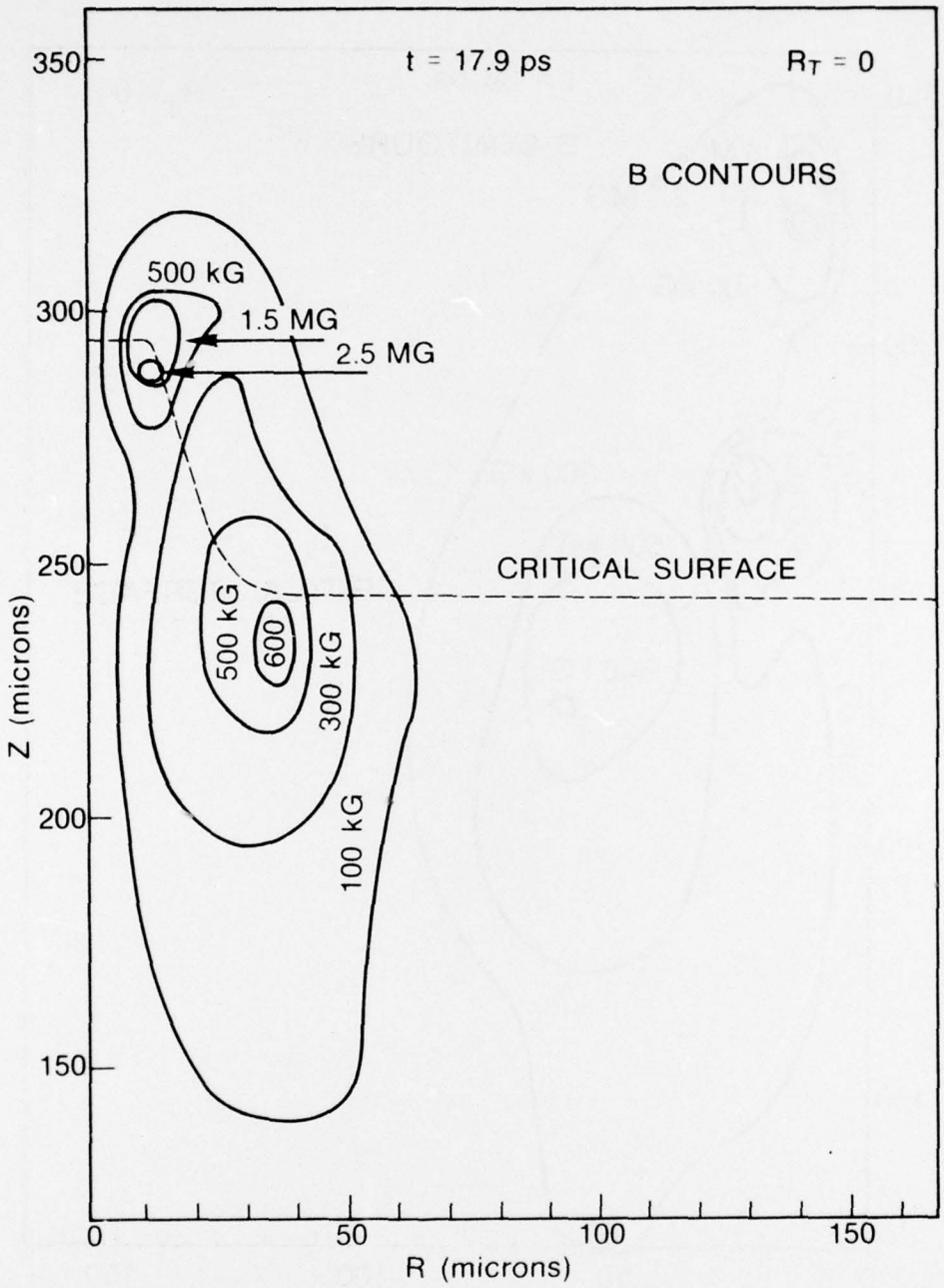

Fig. 1 — Magnetic field contours shortly after peak of laser pulse, no thermal force. Laser pulse is gaussian, FWHM 21 psec, 12μ focal spot, 10^{16} w/cm^2. Carbon target with laser incident from bottom of figure.

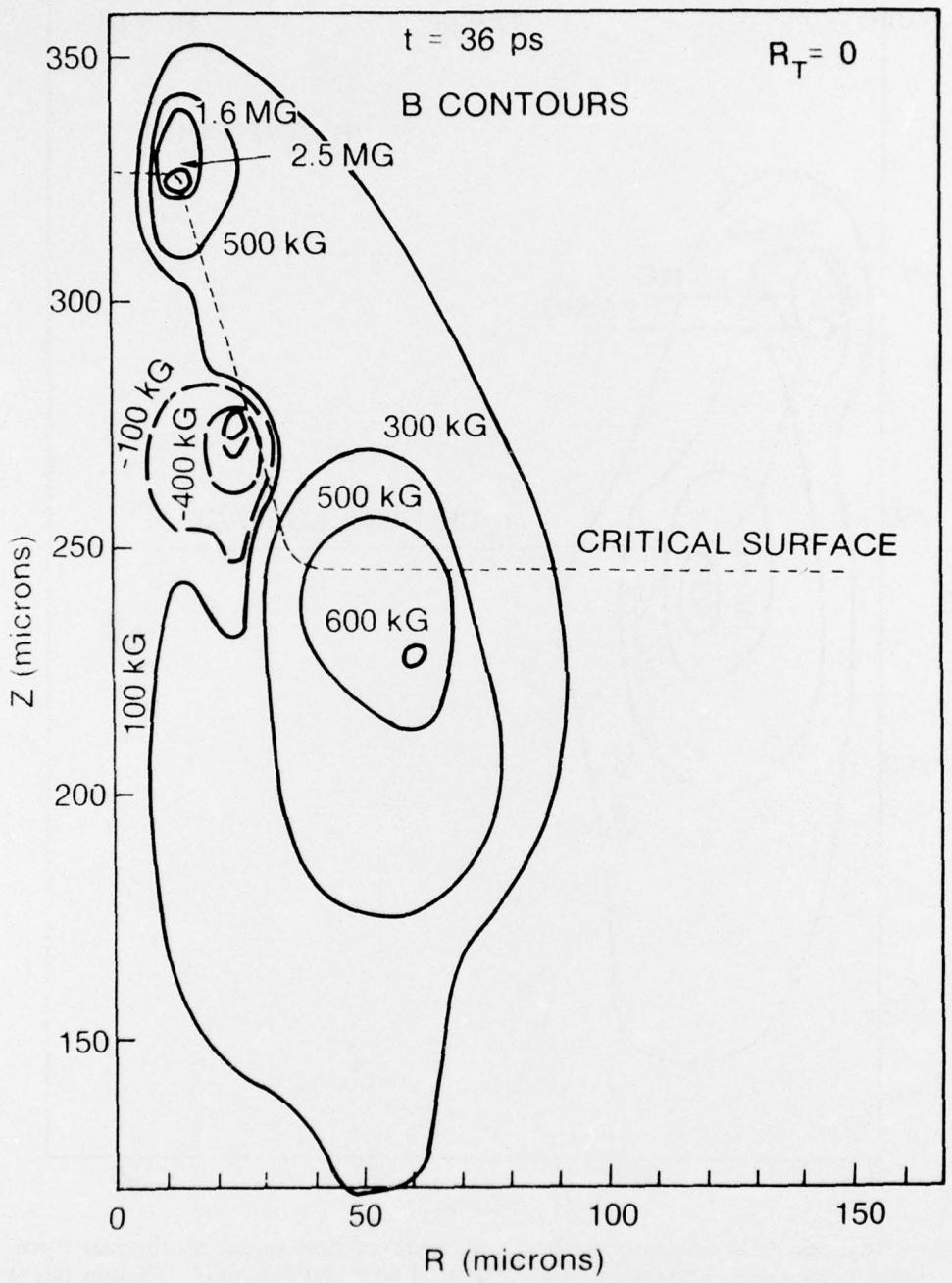

Fig. 2 — Magnetic field somewhat later, same case as Fig. 1. Dotted contours represent negative B.

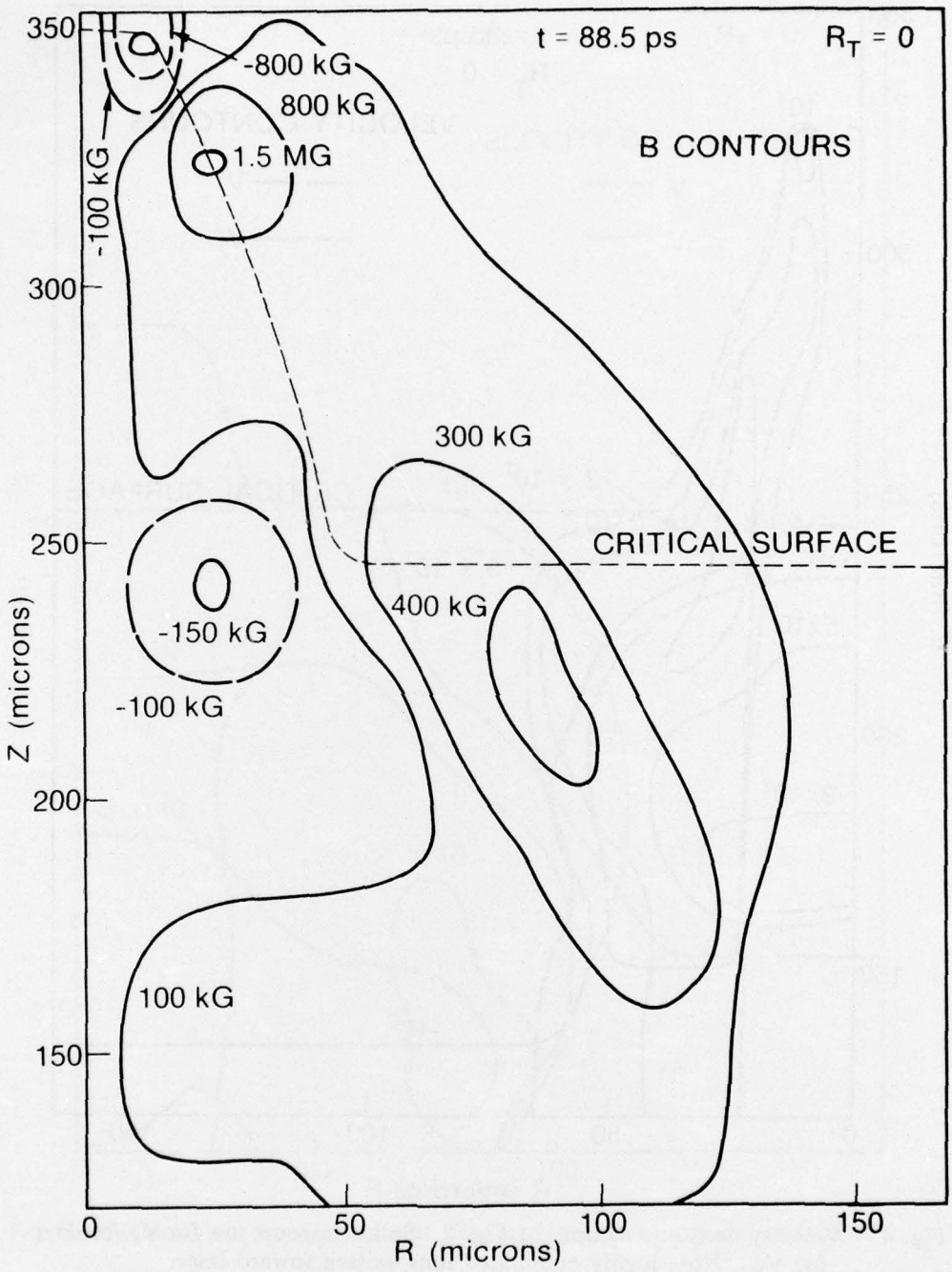

Fig. 3 — Still later. Note complex structure and multiple field reversals.

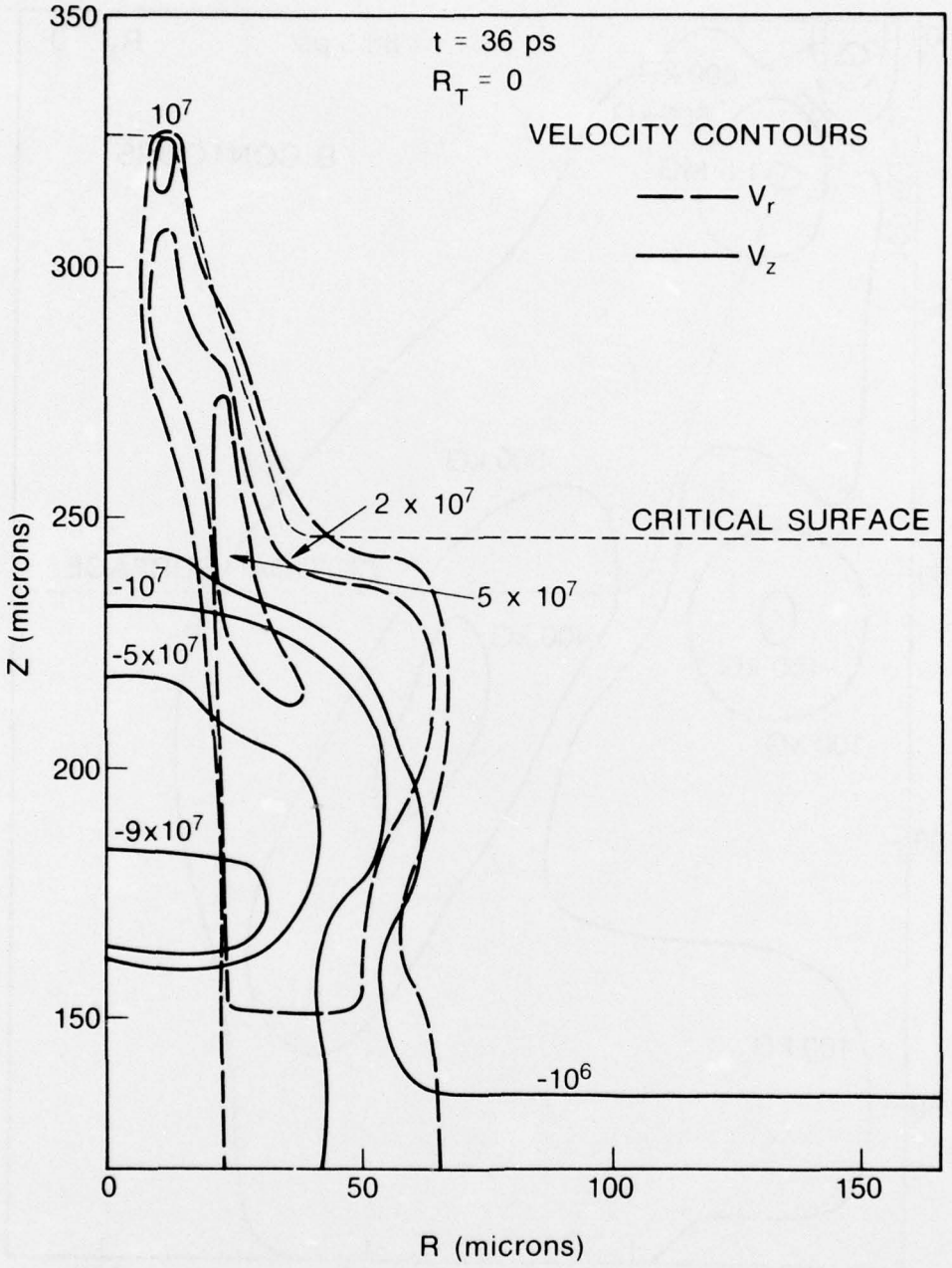

Fig. 4 — Velocity contours at time of Fig. 2. Solid contours are for V_z, broken for V_R. Note highly collimated ions exiting toward laser.

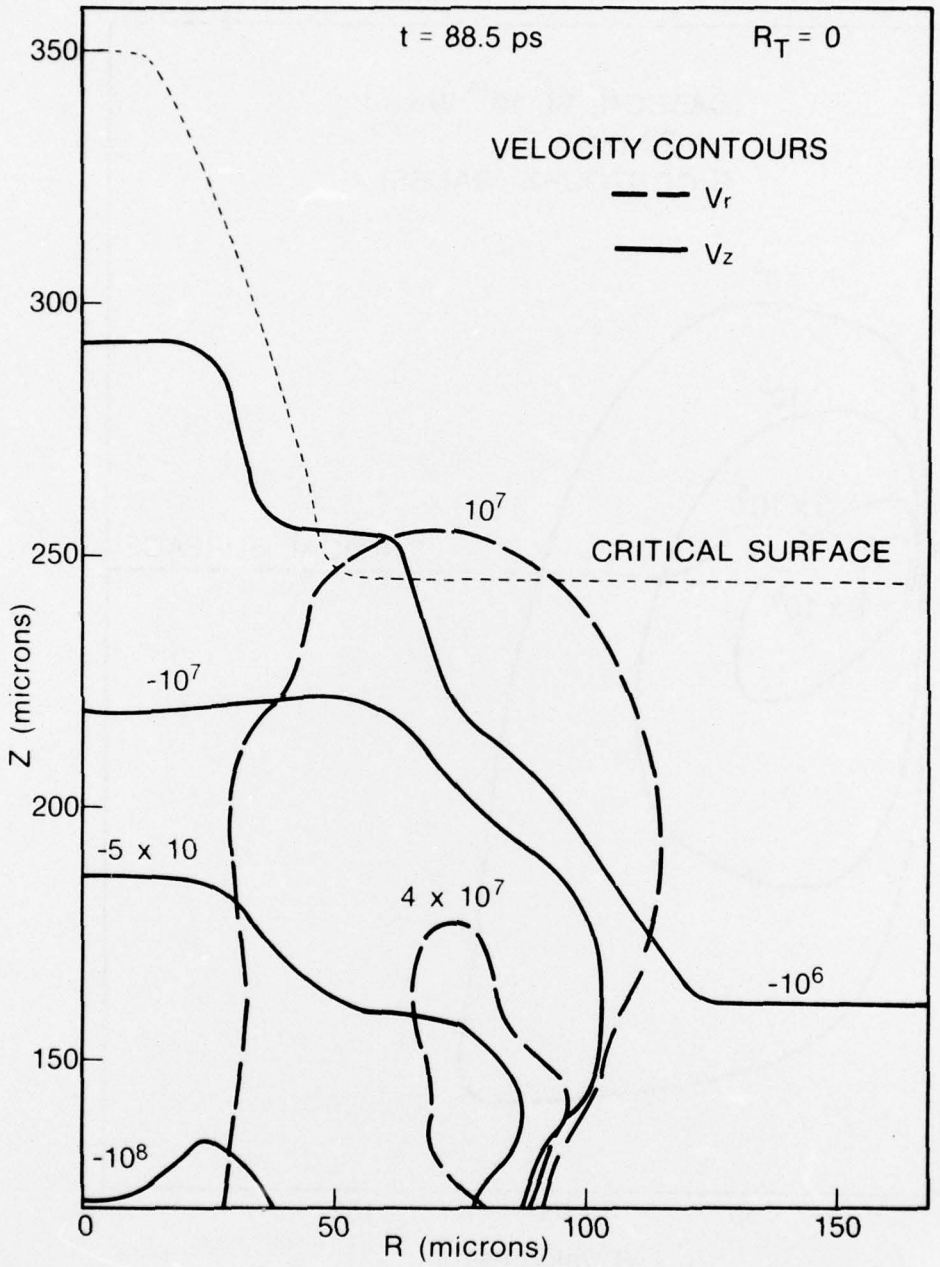

Fig. 5 — Velocity contours at time of Fig. 3. Note beam remains collimated.

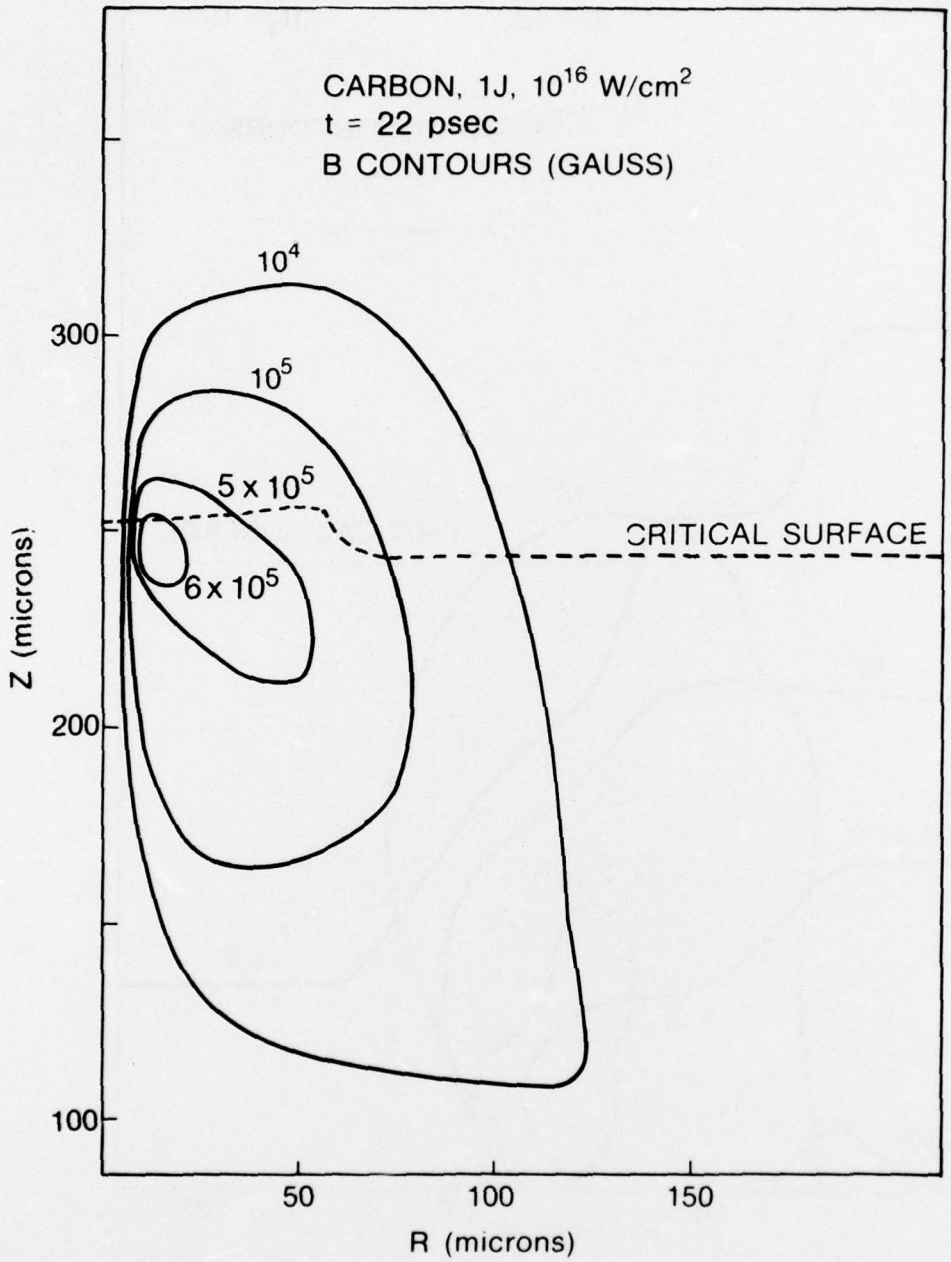

Fig. 6 — Magnetic field contours shortly after peak of laser pulse, complete source term. Same experiment as Figs. 1-5.

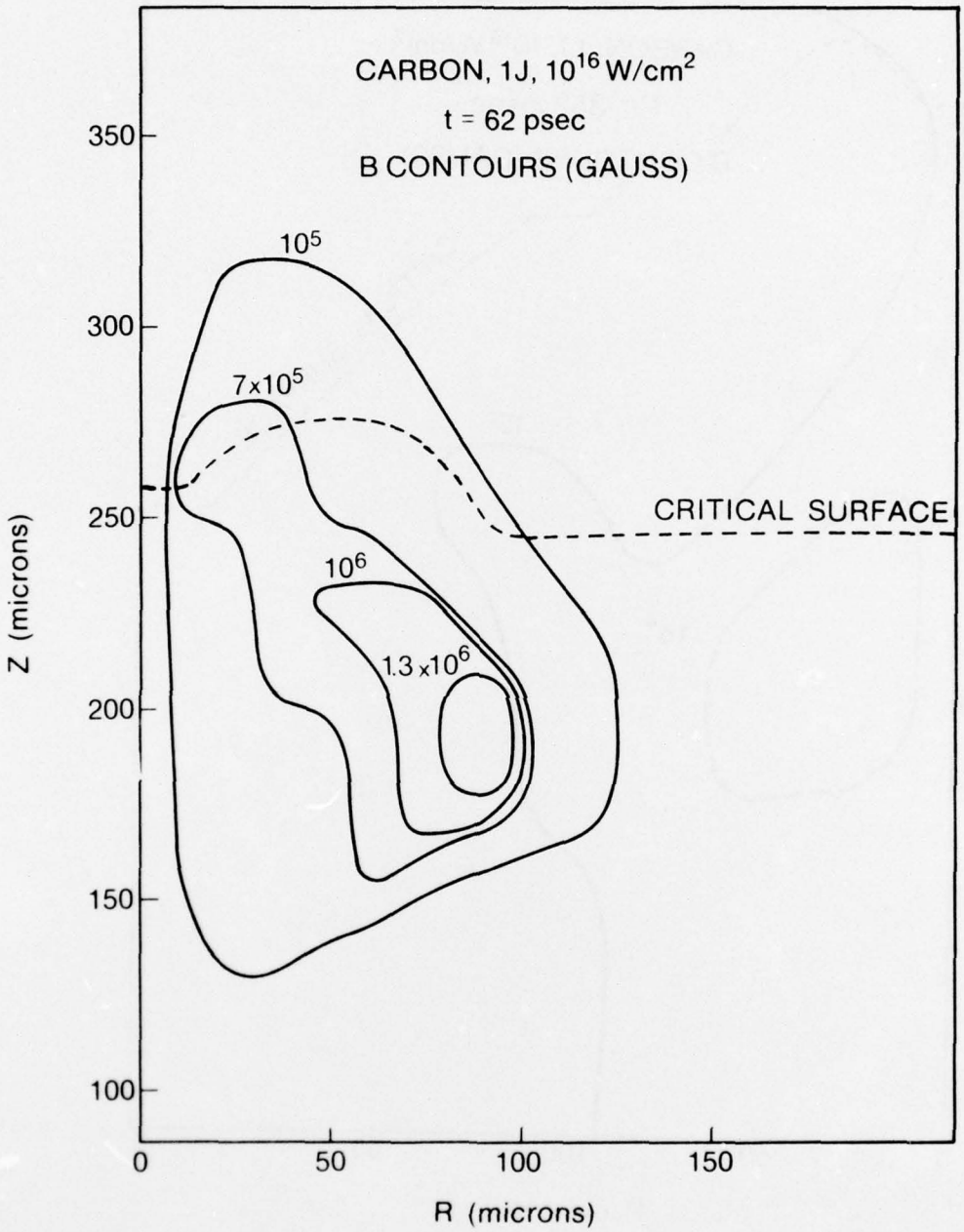

Fig. 7 — Magnetic field much later, case of Fig. 6

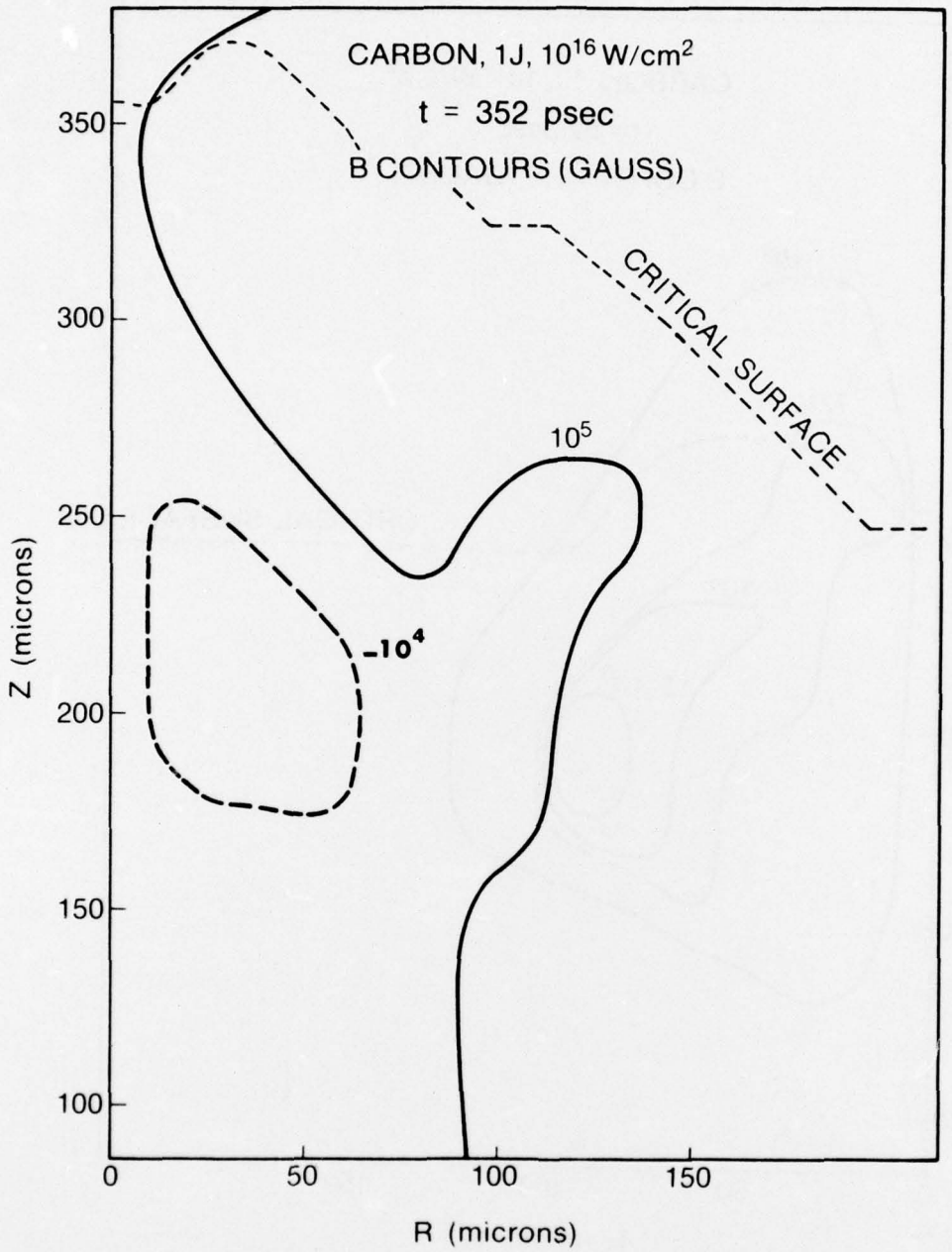

Fig. 8 — Magnetic field very much later, case of Fig. 6. Note long persistence of simple structure.

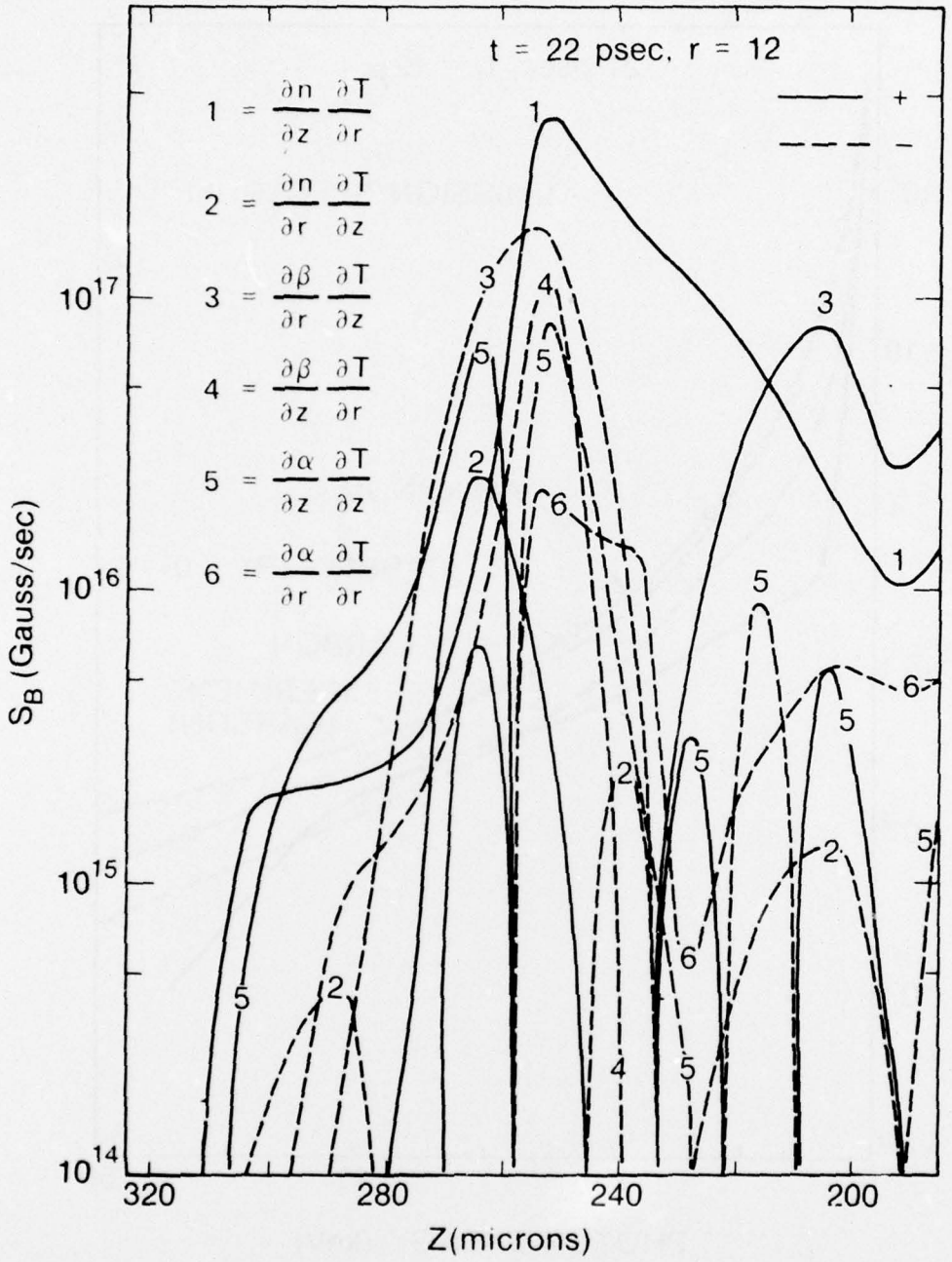

Fig. 9 — Individual contribution to magnetic source versus z, corresponding to a radius of 12μ (through maximum) in Fig. 6. Note that curves 1, 2, and 5 are each dominant in some region.

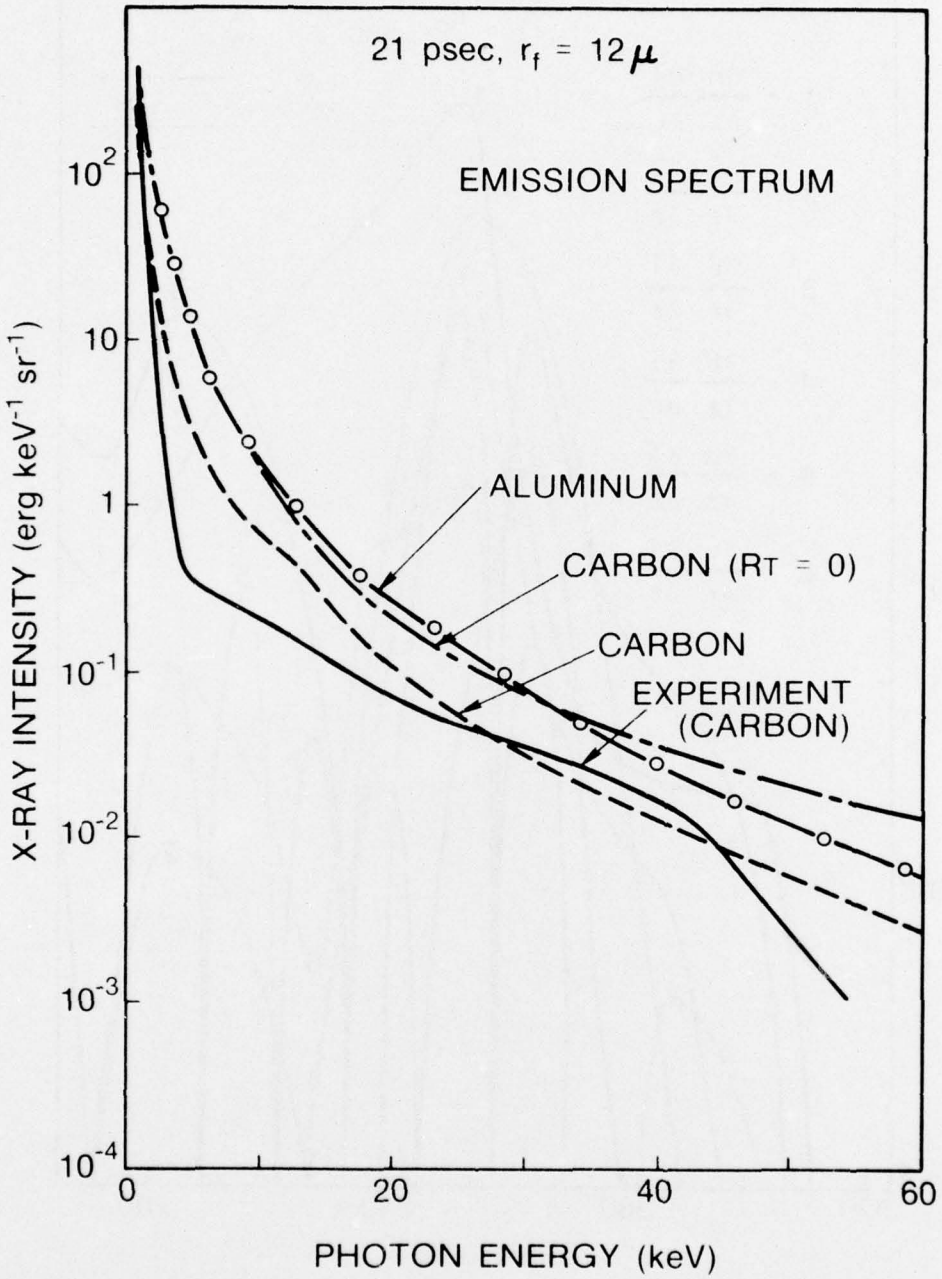

Fig. 10 — Absolute x-ray spectrum from 1 to 60 keV. Solid curve is experiment, broken curve, theory with complete magnetic source term, dashed without thermal force term, and boxes represent change of complete model result due to substitution of Aℓ as target material.

DEPARTMENT OF THE NAVY

NAVAL RESEARCH LABORATORY
Washington, D.C. 20375

OFFICIAL BUSINESS
PENALTY FOR PRIVATE USE, $300

POSTAGE AND FEES PAID
DEPARTMENT OF THE NAVY
DoD-316